Received: 25 August 2023 | Revised: 9 May 2024 | Accepted: 23 June 2024

DOI: 10.1002/pip.3835

RESEARCH ARTICLE

PROGRESS IN PHOTOVOLTAICS WILEY

Cost-efficiency potential of solar energy on a global scale: Case studies for Si solar modules with PERC and heterojunction structures

Tomoya Kobayashi[1] | Hirotaka Katayama[2] | Yosuke Kinden[1] | Yoshitsune Kato[1] | Youichirou Aya[2] | Taiki Hashiguchi[2] | Daiji Kanematsu[2] | Tomonao Kobayashi[3] | Akira Terakawa[2] | Hiroyuki Fujiwara[1]

[1]Department of Electrical, Electronic and Computer Engineering, Gifu University, Gifu, Japan

[2]Energy System Division, Panasonic Corporation, Osaka, Japan

[3]Department of Civil Engineering, Gifu University, Gifu, Japan

Correspondence
Hiroyuki Fujiwara, Department of Electrical, Electronic and Computer Engineering, Gifu University, 1-1 Yanagido, Gifu 501-1193, Japan.
Email: fujiwara.hiroyuki.u7@f.gifu-u.ac.jp

Abstract

Levelized cost of electricity (LCOE) is a crucial metric for assessing the socio-economic cost-efficiency potential of various energy sources including solar photovoltaics. Nevertheless, accurate LCOE estimations for commercialized high-efficiency Si solar modules with passivated emitter and rear cell (PERC) and silicon heterojunction (SHJ) structures have been lacking. In this study, we present the first global LCOE estimates for a PERC module (20% cell efficiency) and a SHJ module (23% cell efficiency), which have been derived by (i) performing rigorous energy-yield calculations with full-spectral and temperature-dependent simulations that incorporate all essential meteorological effects and (ii) considering country-specific capital costs and discount rates. Moreover, to determine the universal global LCOE, the LCOEs for three distinct installation capacities (100 MW for a utility, 500 kW for a commercial, and 5 kW for a residential system) have been unified by selecting an appropriate system size at each location based on a population density. We find that the LCOEs of both PERC and SHJ systems are below 3 cents/kWh in 2020 US dollar in many areas of China, Saudi Arabia, the United States, Australia, Chile, and Botswana, where the conditions of a high energy yield, low population density, low capital cost, and low country-risk premium are satisfied simultaneously. In contrast, many European countries exhibit a moderate LCOE of 3∼5 cents/kWh. Notably, Japan and Russia exhibit quite high LCOEs (6∼10 cents/kWh) primarily due to significantly higher installation costs and moderate energy yields. Importantly, the global LCOEs of the PERC and SHJ modules are quite similar, with the SHJ module showing a slightly better cost performance in the regions near the equator due to its low temperature coefficient. Conversely, the PERC module demonstrates a cost advantage in the Northern Hemisphere due to a lower module cost.

KEYWORDS
country-risk premium, global energy yield, global LCOE, PERC, population density, rigorous energy-yield calculations, silicon heterojunction cell, weighted average capital cost

1 | INTRODUCTION

Economic cost is one of crucial driving factors for the deployment and expansion of renewable energy sources. In evaluating the cost efficiency of various energy sources, levelized cost of electricity (LCOE)[1–4] is generally considered.[4,5] Surprisingly, due to a rapid reduction of Si solar-module prices that occurred in the last two decades,[2,3,6,7] the LCOE of photovoltaic (PV) electricity is now quite low (3 cents/kWh),[4,5] and PV energy becomes one of the most competitive energy sources, realizing grid parity[1] in wider regions.[2] Now, solar energy is a primary choice for many countries, accounting for 65% of total renewable capacity expansion in 2022,[8] even though the potential of solar energy is widely underestimated.[9]

Nevertheless, solar-module power generation is influenced strongly by local meteorological conditions, and thus, the solar-energy LCOE is a location specific value. Moreover, a solar-module LCOE varies strongly with a device configuration[10,11] (i.e., structure), installation size (i.e., residential, commercial, and utility scale),[12] and the economic situation of country,[13,14] such as discount rate (or interest rate). Thus, it is generally quite challenging to grasp the global LCOE, even though the evaluation of such a world-wide LCOE map is of considerable importance to design a future renewable electricity grid to cope with climate crisis. So far, several studies have devoted to calculating world solar-energy LCOEs.[13–16] In these studies, however, the LCOE has been calculated by simplified manners based on meteorological data without considering device physics.

As high-efficiency Si solar cell modules, on the other hands, two types of solar cells have been produced widely: i.e., a passivated emitter and rear cell (PERC)[17–19] and silicon heterojunction (SHJ)[20–22] cell. Although the conversion efficiency of a SHJ cell (26.8%)[22] is higher than a PERC solar cell (24.5%),[23] currently, PERC is the most produced type of solar cells.[7,17,18] Quite interestingly, the cell costs of PERC and SHJ devices are similar,[10] but the temperature coefficient of SHJ cells[21] is notably better, compared with PERC solar cells.[24–26] Thus, an interesting and important issue is which type of solar cell shows better (lower) LCOE globally. To answer this question, quite detailed device simulations need to be performed for different locations worldwide.

In our previous study, we assessed the global energy yields of SHJ single and perovskite/SHJ tandem modules by establishing a new rigorous self-consistent model that performs full spectral calculations incorporating all fundamental time-varying parameters affecting the module power output.[27] In particular, the temperature dependences of the optical and electrical characteristics are modeled explicitly, and reliable model parameters are extracted from an industry-compatible SHJ cell. Based on the global energy yield obtained, the global LCOE can further be evaluated. The above modeling scheme can also be applied to a PERC configuration to estimate the world PERC LCOE, which allows us to determine which region is more suitable for a SHJ or PERC solar module.

In this study, we have addressed the issues that have not been answered before: what are the accurate global LCOEs of PERC and SHJ modules and how does the LCOE ratio of PERC/SHJ vary globally? To implement accurate energy-yield calculations, we have performed full device simulations for a commercial PERC solar cell with external quantum efficiency (EQE) calculation and temperature-dependent device parameter modeling. For the LCOE calculation, we have developed a new formalism that considers all the essential factors including (i) world population density, which determines a proper solar-module installation size (utility/commercial/residential), and (ii) country-dependent capital expenditure and (iii) country-dependent weighted average capital cost (WACC), to best represent the global LCOE. We have determined global LCOEs for PERC and SHJ devices for the first time and confirmed that the SHJ module exhibits slightly better cost performance in countries located near equator, whereas PERC shows slightly lower LCOE in northern countries (Canada, Sweden, etc.).

2 | ASSESSMENT OF GLOBAL LCOE

2.1 | Device structures

Figure 1 represents the structures of monocrystalline monofacial Si solar devices with (A) PERC and (B) SHJ configurations applied for global LCOE calculations. The conversion efficiency (η) of the PERC cell, from which the temperature-dependent device parameters are extracted, is 20.37% with the short-circuit current density (J_{sc}) of 38.8 mA/cm^2, open-circuit voltage (V_{oc}) of 0.664 V, and fill factor (FF) of 79.0%. The structure and characteristics of the SHJ cell ($\eta = 23.27\%$, $J_{sc} = 38.5$ mA/cm^2, $V_{oc} = 0.745$ V, and FF = 81.1%) were adopted from our previous study.[27] The layer thicknesses shown in Figure 1 correspond to those obtained from the optical simulation analyses of the real cells.

The PERC device in Figure 1 has a standard structure with an Al_2O_3 passivation layer and a SiN_x capping layer in the rear[18] and SiN_x/SiO_2 front contact layers. In the rear, the local back-surface field (BSF) p^+ structure is formed by Al diffusion. In the analyzed commercial SHJ cell, hydrogenated amorphous silicon (a-Si:H) passivation and doped layers are provided in the front and rear sides, contacted by In_2O_3:W (IWO) transparent conductive oxide (TCO) layers.

For the optical device simulation of the PERC solar cell, the optical constants reported in Fujiwara and Collins[28] were adopted. In the energy yield calculation of each type of solar modules, a structure of glass/ethylene vinyl acetate (EVA)/cell was considered.

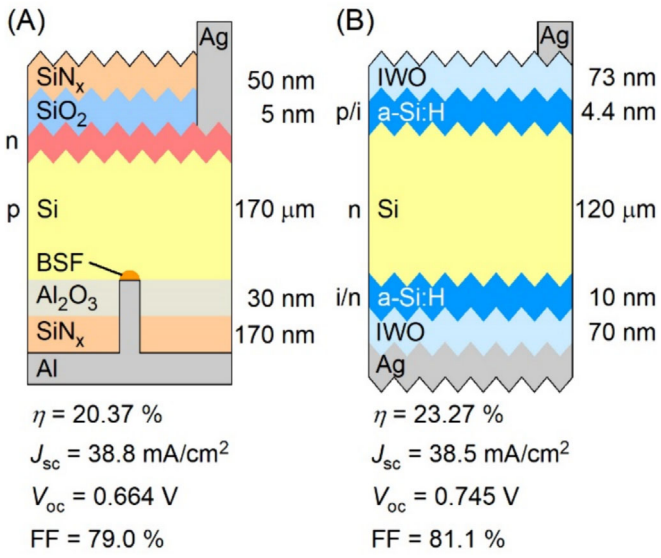

FIGURE 1 Structures of monocrystalline monofacial Si solar devices with (A) PERC and (B) SHJ configurations considered in this study. The conversion efficiencies and the solar characteristics of the PERC and SHJ cells are also indicated. The layer thicknesses shown in Figure 1 correspond to those obtained from the optical simulation analyses of the real cells, and the thickness of hydrogenated amorphous silicon (a-Si:H) front layers (p/i layers) is slightly underestimated. The IWO in the SHJ cell indicates In_2O_3:W transparent conductive oxide.

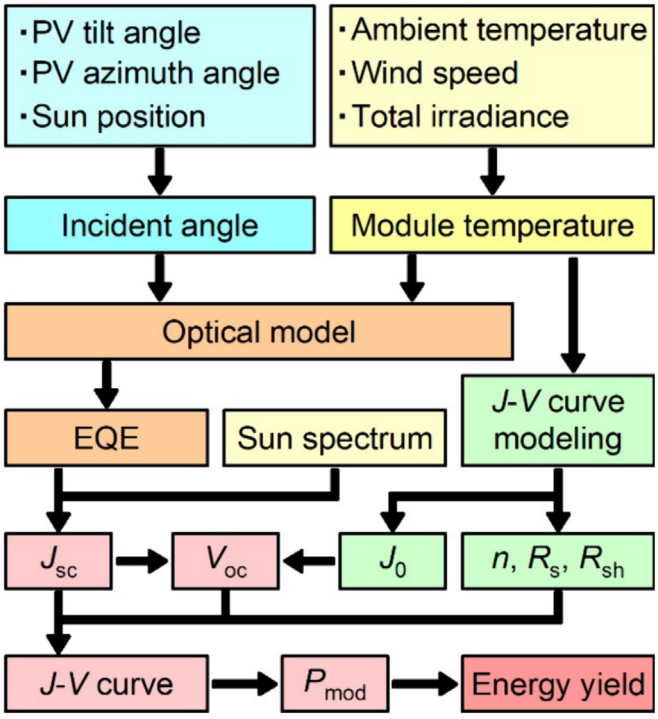

FIGURE 2 Calculation procedure of annual energy yields of the PERC and SHJ modules. The exact procedure is described in our previous study.[27] The P_{mod} denotes the maximum module power density.

2.2 | Energy yield calculation

The energy yield calculation in this study is based on the exact same scheme reported in our previous study.[27] Figure 2 briefly explains the calculation procedure. From the solar panel setting conditions and the time-varying Sun position, a module incident angle (θ_{in}) is determined. Specifically, solar panels are oriented toward south in the Northern Hemisphere and north in the Southern Hemisphere, whereas the PV tilt angle is treated equivalent to the latitude of a calculated place. From the meteorological data (ambient temperature, wind speed, and total irradiance), the module temperature (T) is estimated.

The θ_{in} and T are two main variables in the optical calculation, and the optical constants of the crystalline silicon absorber vary with T.[27] From the optical simulation, we calculate the EQE spectrum, from which J_{sc} is determined. From the T-dependent J-V curve, the device parameters of the saturation current density (J_0), diode factor (n), series resistance (R_s), and shunt resistance (R_{sh}) are extracted and modeled for T. The V_{oc} of the cell can be calculated from J_{sc} and J_0. Finally, from five T-dependent parameters of $J_{sc}(T)$, $V_{oc}(T)$, $n(T)$, $R_s(T)$, $R_{sh}(T)$, the J-V curve at θ_{in}, and T is derived, from which the maximum module power density (P_{mod}) and the energy yield are calculated. As confirmed above, in our scheme, a full spectral calculation is performed to obtain an accurate energy yield by considering hourly varying Sun spectra, θ_{in}, and T. To calculate the module energy yield, we consider the cell area factor of 0.94 in a module structure (glass/EVA/cell), and, as a result, the module efficiencies of the PERC and SHJ devices become $\eta_{PERC} = 18.60\%$ and $\eta_{SHJ} = 20.91\%$, respectively.

The annual energy yield of the PERC module was calculated by integrating P_{mod} at 762 points in North and South America based on hourly irradiance spectra and meteorological data, obtained from the National Solar Radiation Database (NSRDB)[29] developed by NREL for the year 2018. This database summarizes Sun spectra under clear-sky or cloudy-sky conditions, calculated by applying the Fast All-sky Radiation Model for Solar applications with Narrowband Irradiances on Tilted surfaces (FARMS-NIT).[30,31] In our simulation, 8,760 spectra are employed for the prediction of an annual energy yield of one place, and such a calculation is repeated for a total of 762 places in America.

2.3 | LCOE calculation

To determine the global LCOE, we have applied the following equation:

$$\mathrm{LCOE} = \frac{C_L}{Y_L} = \frac{s_j I_{0,k} + \sum_{t=1}^{U} \frac{m_j O_k}{(1+r_j)^t}}{\sum_{t=1}^{U} \frac{Y_0(1-d)^t}{(1+r_j)^t}}. \quad (1)$$

In essence, the LCOE of solar modules is calculated from the division of the module lifetime cost (C_L) by the lifetime energy yield

(Y_L). Specifically, C_L is derived from a capital cost (I_0), operating and maintenance cost (O), and discount rate (r) for a lifetime of the system ($U = 25$ years), whereas Y_L is determined from an initial energy yield (Y_0), degradation rate (d), and r. In Equation (1), s_j is a country-specific scale parameter for an installation cost, and $s_j I_0$ is equivalent to the capital cost in a country j. Similarly, m_j indicates the scale parameter for the operating and maintenance cost for the country j. Moreover, r is also taken as a country dependent value (i.e., r_j). The subscript k for I_0 and O ($k = 1 \sim 3$) indicates that three different values are adopted for utility (100 MW; $k = 1$), commercial (500 kW; $k = 2$), and residential (5 kW; $k = 3$) facilities. For the LCOE calculation of solar modules, slightly different formulas have been applied so far,[1,3,4,13,15,16] and Equation (1) is essentially similar to the one proposed by Fraunhofer Institute.[3,4] In this study, however, the unique values of the country (i.e., s_j and r_j) and types of facilities (i.e., k) are considered explicitly.

For the calculation of I_0, we first derived the cell costs of PERC (23.53 \$/m^2) and SHJ (29.23 \$/m^2) in 2020 US dollar based on the report of Messmer et al.[10] using a year average exchange rate of 1 € = 1.1422\$.[32] Based on the same reference,[10] we estimate a module fabrication cost of 26.26 \$/m^2, which results in the total module costs of 49.79 \$/m^2 (PERC) and 55.49 \$/m^2 (SHJ). The other peripheral costs including inverter, balance of system (BOS), and soft-BOS for different installation sizes ($k = 1 \sim 3$) were deduced for the United States from the detailed procedure reported by NREL.[12] For this calculation, however, we performed slight adjustments due to a small difference between our module efficiencies ($\eta_{PERC} = 18.60\%$ and $\eta_{SHJ} = 20.91\%$) and the reference value ($\eta_{ref} = 19.9\%$) according to the criteria (area, capacity, and average) of Zafoschnig et al.[11]

Unfortunately, $I_{0,k}$ values, estimated specifically for the United States in this study, change according to the social and economic situation of each country and cannot be treated as unique values. Thus, to reflect the country-dependent situation for solar-panel installations, we have included the scale parameter s_j in Equation (1). Specifically, we have calculated s of each country based on quite detailed estimation of country specific installation costs reported by IRENA.[33] In particular, s_j was calculated using an expression of $s_j = I_{0,j}/I_{0,USA}$, where $I_{0,USA}$ is I_0 for a utility-scale PV system (i.e., $I_{0,1}$) in the United States and $I_{0,j}$ indicates those in other countries provided by IRENA. In IRENA's report,[33] however, the installation costs are available for only 37 countries, and, for the other countries, we have applied a world-weighted-average value ($s = 0.802$) derived from the installation capacity. The actual s_j values used in our calculations are summarized in Figure S1. Note that $s_j < 1$ in many countries, and thus, the initial installation cost is cheaper than the United States, while Russia ($s = 1.72$) and Japan ($s = 1.66$) exhibit quite high values.

The operating and maintenance costs for the systems $k = 1 \sim 3$ (O_k) are calculated for the United States based on the NREL report,[12] and their categories and values are shown in Table S1. For this calculation, slight adjustments of the cost values have also been made by reflecting the actual efficiencies of our solar devices. For m_j, however, the detailed data do not exist, and we simply assumed $m_j = 1$ in the member countries of the OECD (organization for economic co-operation and development), whereas $m_j = 0.51$ is assumed for non-member countries of the OECD, based on the criteria and values reported by IRENA.[33]

The country-specific r_j used in Equation (1) is quite important and modifies LCOE rather significantly.[13] In general, r has been treated equivalent to a weighted average capital cost (WACC) as $r_j = r_{WACC,j}$.[2–4,10,11,13,33] Nevertheless, the calculation of the country-dependent WACCs is essentially difficult,[13] and there has been intense discussion for appropriate WACCs that should be used for the cost calculation.[34,35] In the early reports of IRENA[33] and IEA,[36] rather simple assumptions were made; in the case of IRENA, $r_{WACC} = 0.05$ for the member countries of the OECD and China, whereas $r_{WACC} = 0.075$ for the other countries. In the recent report of IRENA, country-specific WACCs are considered.[37] It should be emphasized that WACC is essentially a financial rate that is required to pay to compensate the necessary costs of equity and debt and increases drastically in a country with a higher inflation.[13,34] To determine country-specific WACCs, the application of a country risk premium corresponding to Moody's country rating has been proposed[34]:

$$r_{WACC} = r_{risk} + r_0, \tag{2}$$

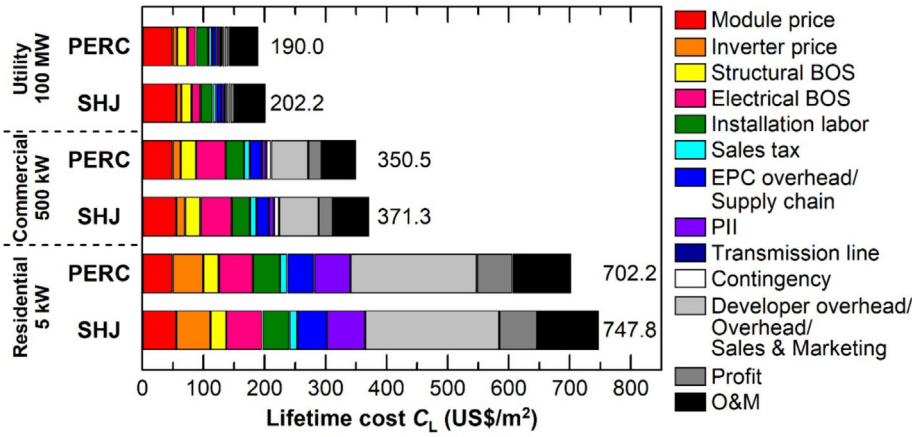

FIGURE 3 Lifetime cost (C_L) of the PERC and SHJ modules in the unit of \$/m^2 (2020 US dollar) for three distinct installation capacities of utility (100 MW), commercial (500 kW), and residential (5 kW) systems in the United States ($s_j = 1$, $r_j = 3.1\%$, $m_j = 1$, $U = 25$ years). The numerical values and exact categories of Figure 3 can be found in Table S1. In the figure, the following abbreviations have been used: BOS (balance of system), EPC (engineering, procurement, and construction), PII (permitting, inspection, and interconnection), and O&M (operation and maintenance).

where r_{risk} is the country risk premium and r_0 shows a baseline rate in a risk-free case. It should be noted that $r_{risk} = 0$ in many developed countries, and, for r_0, a value of 3.1% derived from a 10-year average cost for various solar systems in Germany[38] has been proposed.[34] In this study, we calculated $r_j = r_{WACC,j}$ according to Equation (2) using $r_0 = 3.1\%$ with r_{risk} for the year 2020[39] and used $r_{WACC} = 7.5\%$ for the few countries with no r_{risk} data. The r_{WACC} in the globe used in our calculation is shown in Figure S2 and is essentially consistent with the trend reported in recent IRENA's report.[37]

Figure 3 summarizes C_L of Equation (1) in the unit of \$/m^2 for the PERC and SHJ systems in the United States ($s_j = 1$, $r_j = 3.1\%$, $m_j = 1$, $U = 25$ years) in the year 2020, estimated from the above procedures and assumptions. The numerical values of Figure 3 can be found in Table S2. In the figure, the C_L values for three different system sizes (i.e., $k = 1 \sim 3$) are shown, and the cost categories have been adopted from the work of NREL.[12] It can be seen that C_L changes drastically with the system size, and the small residential system costs more than three times higher than that of the utility-scale facility. In all cases, module costs are equal, but the other costs change rather significantly. It should be mentioned that the C_L values of PERC and SHJ are quite similar, although the SHJ systems show slightly higher costs than those of the PERC systems. For the residential system, for example, the inverter price for SHJ is slightly higher than that for PERC, because the power generation in a square meter is higher in the SHJ panel due to a higher efficiency, which in turn increases a cost for the inverter (i.e., \$/W).

In the calculation of Y_L using Equation (1), d plays a significant role, and the choice of the proper d is important. In particular, PERC devices exhibit a relatively large initial degradation in the first year,[18,40–42] and thus, $t = 1$, rather than $t = 0$, has been assumed in Equation (1). For the PERC system in this study, we assumed the initial degradation of 2.0%[41,42] with the following continuous degradation of 0.36%[43] applied from the second and later years. For the SHJ device, based on the systematic work of Jordan et al.,[44] a constant value of $d = 1.0\%$ was adopted.

Figure 4A shows the degradation of the PERC and SHJ devices, calculated from $(1 - d)^t$ under the above assumptions. During the lifetime of the system (i.e., $U = 25$ years), the SHJ system exhibits a larger degradation, and the module efficiency becomes 77.8% of the initial at $U = 25$ years, whereas the PERC module shows an improved stability with the final efficiency of 89.8% of the initial value. On the other hand, Figure 4B shows the annual energy-yield factor, obtained from $(1 - d)^t/(1 + r)^t$ assuming d of Figure 4A and $r = 0.05$. Due to the lower degradation rate, the PERC system shows a slightly higher energy-yield factor at $U = 25$ years, compared to the SHJ system.

As described above, we assumed three different solar-panel installation sizes ($k = 1 \sim 3$). As a result, from the calculations using Equation (1), three corresponding LCOE values are obtained. In this study, to estimate the reasonable LCOE in a global scale, we assigned the proper installation size at each location simply using a population density in the area. Specifically, in city areas with high population densities, the installation of utility scale systems is difficult, and thus, the residential systems are more proper, while in the rural areas, the trend becomes opposite. Accordingly, based on the criteria of the national census in the United States (2010),[45] we set two boundaries of 1,000 persons per square mile (or 386 person/km^2) and 500 person/mi^2 (193 person/km^2) for the world population. The location with >1,000 person/mi^2 defines a city area where the residential LCOE is shown, and the area with <500 persons/mi^2 characterizes a rural area where the utility scale facility is placed. In the region with middle densities (i.e., 500 < x < 1,000 person/mi^2), we placed a commercial-scale system. Although the above new approach is quite simple, the result is expected to reflect the reality of the global LCOE.

For the population density of the world, we adopted values reported in the global database[46] (Figure S3), and the distinct installation capacity at each location, calculated from our categorization using the world population density, is shown in Figure S4. It can be seen that for the most areas, the utility system is assumed, whereas the residential and commercial systems are considered mainly in India, the east side of China, and some parts of EU nations and Japan.

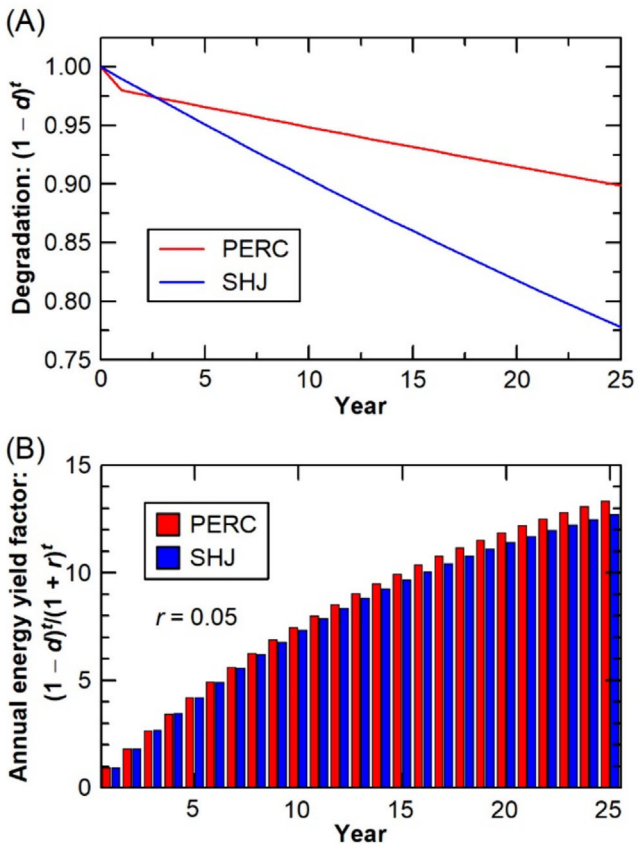

FIGURE 4 (A) Assumed degradation of the PERC and SHJ devices over 25 years and (B) annual energy-yield factors of the PERC and SHJ modules, calculated from $(1 - d)^t/(1 + r)^t$ with $r = 0.05$. For the PERC system, an initial degradation of 2.0% in the first year,[41,42] followed by an annual degradation rate of 0.36%,[43] is considered. For the SHJ device, a constant yearly degradation of $d = 1.0\%$[44] is assumed.

3 | RESULTS

3.1 | Modeling of the PERC device

Figure 5 summarizes the experimental and modeling results of the PERC cell shown in Figure 1A: (A) temperature variation of the experimental EQE spectrum (open circles) and their modeling results (solid lines), (B) temperature variation of the experimental *J*-*V* curve (open circles) and the fitted results (solid lines), (C) experimental temperature-dependent J_0 (open circles) and modeled variation (solid lines), and (D) power densities of the PERC and SHJ modules and P_{mod} ratio ($P_{mod,SHJ}/P_{mod,PERC}$) as a function of module temperature.

In Figure 5A, the EQE response in the longer wavelength region is extended with increasing *T* due to the bandgap reduction at higher *T*.[47] The solid lines indicate the simulation results calculated from our two-dimensional optical simulation method (double-reflection model: DRM[27,48]). Our simulations reproduce the measured EQE and reflectance (*R*) spectra almost perfectly, when two arbitrary model parameters of DRM are adjusted to $s = 1.93$ and $f = 1.80$, allowing us to calculate accurate J_{sc} values for different temperatures.

In the *J*(*T*)-*V*(*T*) characteristics shown in Figure 5B, large reduction of V_{oc} and slight increase in J_{sc} can be confirmed. From the fitting analyses of each curve assuming a single diode model, five device parameters of J_{sc}, V_{oc}, R_s, R_{sh}, and *n* were extracted for each *T*.[27] In particular, the extracted $R_s(T)$, $R_{sh}(T)$, and $n(T)$ can be expressed by simple linear or constant contributions, which are different from those of the SHJ device (Figure S5). Quite interestingly, the PERC device shows higher R_s, R_{sh}, and *n*, compared with the SHJ structure. The R_{sh} of 4 kΩcm^2, observed for the PERC device, is notably higher, compared with $R_{sh} \sim 1$ kΩcm^2 in the SHJ device.

In Figure 5C, $J_0(T)$ values of the PERC and SHJ structures are shown. The J_0 at each *T* is calculated from the V_{oc} and J_{sc} of the corresponding *J*-*V* curve using a well-known formula of $J_{sc} = J_0[\exp(eV_{oc}/k_BT) - 1]$. In general, $J_0 = J_{0,rad} + J_{0,nonrad}$,[49] where $J_{0,rad}$ and $J_{0,nonrad}$ indicate the radiative and nonradiative components, respectively. In the case of crystalline Si solar cells, $J_{0,nonrad}$ is far larger than $J_{0,rad}$ due to strong Auger recombination[50,51] and thus $J_0 \sim J_{0,nonrad}$.[27] However, $J_{0,nonrad}$ includes the various contributions of Auger, interface, and Shockley-Read-Hall (bulk) recombination. Unfortunately, the separation of these contributions, particularly the separation of the interface and bulk recombination,[52] is quite difficult. In our previous study,[27] therefore, we have modeled $J_{0,nonrad}$ as $J_0 = J_{0,nonrad} = eA\exp(B/k_BT)$, shown by the solid lines in Figure 5C. Here, *A* and *B* are adjustable parameters; the parameter *A* expresses the baseline J_0 of the device, whereas the parameter *B* indicates the temperature-dependent variable. The PERC device shows a substantially higher J_0 because of stronger interface recombination (or higher *A* value of 1.63×10^{30} s^{-1} cm^{-2}), compared with the SHJ device ($A = 3.84 \times 10^{29}$ s^{-1} cm^{-2}). In particular, as confirmed from Figure 1, the V_{oc} of the PERC cell is notably smaller than that of the SHJ cell,[53] which is consistent with the large interface recombination in the PERC cell. On the other hand, the *T*-dependent contributions of the PERC and SHJ structures ($B_{PERC} = -1.99 \times 10^{-19}$ J, $B_{SHJ} = -2.06 \times 10^{-19}$ J) are similar. Note that, in our model shown in

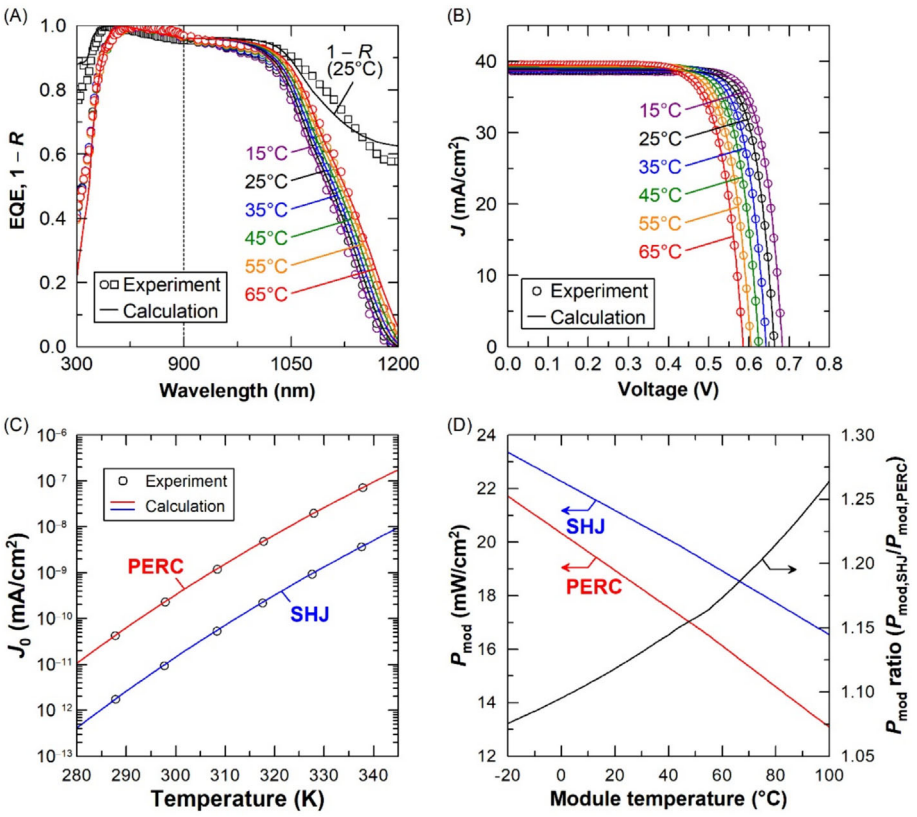

FIGURE 5 Temperature variations of (A) EQE, (B) *J*-*V* curve, (C) J_0, and (D) maximum module power density (P_{mod}), obtained for the 20.37%-efficient PERC cell. The open circles show the experimentally derived data, whereas solid lines indicate the fitted results obtained from optical and electrical simulations. In (A), the open squares show the experimental $1 - R$ data (25°C), and the corresponding simulation result is also shown.

Figure 2, we estimate $V_{oc}(T)$ from $J_{sc}(T)$ obtained from the EQE calculation and $J_0(T)$ shown in Figure 5C.

In Figure 5D, the calculated P_{mod} decreases notably with increasing T, and the SHJ module exhibits higher P_{mod} than that of the PERC module because of the lower temperature coefficient of the SHJ module.[20,21] In the figure, the P_{mod} ratio increases sharply as T increases, indicating the simple fact that the SHJ module becomes more preferable when the module is placed in a warmer region.

The better temperature coefficient in SHJ, compared with the PERC cell, can be interpreted partly by preferable R_s and n variations with T, as extracted in this study (Figure S5). Specifically, R_s in the SHJ cell decreases with T due to the enhanced conductivity in a-Si:H layers at higher T,[54] while the R_s of the PERC cell increases with T. The n of the SHJ cell also shows the improved value at higher T, whereas the n of the PERC cell increases with T. Moreover, our simple calculation shows that the smaller J_0 in SHJ further reduces the temperature coefficient of V_{oc}. These effects contribute to increase the P_{mod} ratio at higher T.

3.2 | Limiting factor of the PERC device

The detailed optical and electrical simulations for the PERC cell shown in Figure 5 further allow us to determine the efficiency loss mechanism of the PERC cell. Thus, by following the procedure reported earlier,[49] we have estimated the efficiency loss theoretically. Figure 6 summarizes the cause of the efficiency reductions categorized by J_{sc}, V_{oc}, and FF losses at room temperature. The Shockley–Queisser[55] limit obtained for the bandgap of Si (1.11 eV) is 33.44%, while the performance of the PERC cell is 20.30%. The difference between these efficiencies can be attributed to the effects of J_{sc} (4.04%), J_0 (7.77%), resistivity of R_s and R_{sh} (0.48%), and n (0.85%). The EQE simulation further determines the efficiency losses caused by each constituent layer. The J_{sc} loss can mainly be attributed to the shadow loss of the electrode, reflection loss, and absorption loss in Al back electrode. However, the largest loss in the PERC device occurs by the significant increase in $J_{0,nonrad}$ due to the interface recombination.

We have performed a similar analysis for the SHJ device in Figure 1B using the device parameters reported in our previous study[27] (Figure S6). The above analyses show that the difference between the PERC and SHJ efficiencies (~3%) can be attributed solely to the suppression of $J_{0,nonrad}$ with similar J_{sc} loss (4%) and FF loss (1%) for the PERC and SHJ devices.

Previously, Richter et al.[56] derived a theoretical efficiency limit of 29.43% for a Si solar cell with a 110 μm thick wafer based on a quite detailed theoretical model. For this result, the detailed analysis for the efficiency gap observed in a PERC device has also been reported,[57] which is essentially consistent with the result shown in Figure 6.

3.3 | Energy yield of the PERC device

Figure 7A shows the annual energy yields of the PERC module placed in North and South America, calculated explicitly from the model of Figure 2 by applying hourly meteorological data of each place. The energy yield varies considerably depending on the location and is

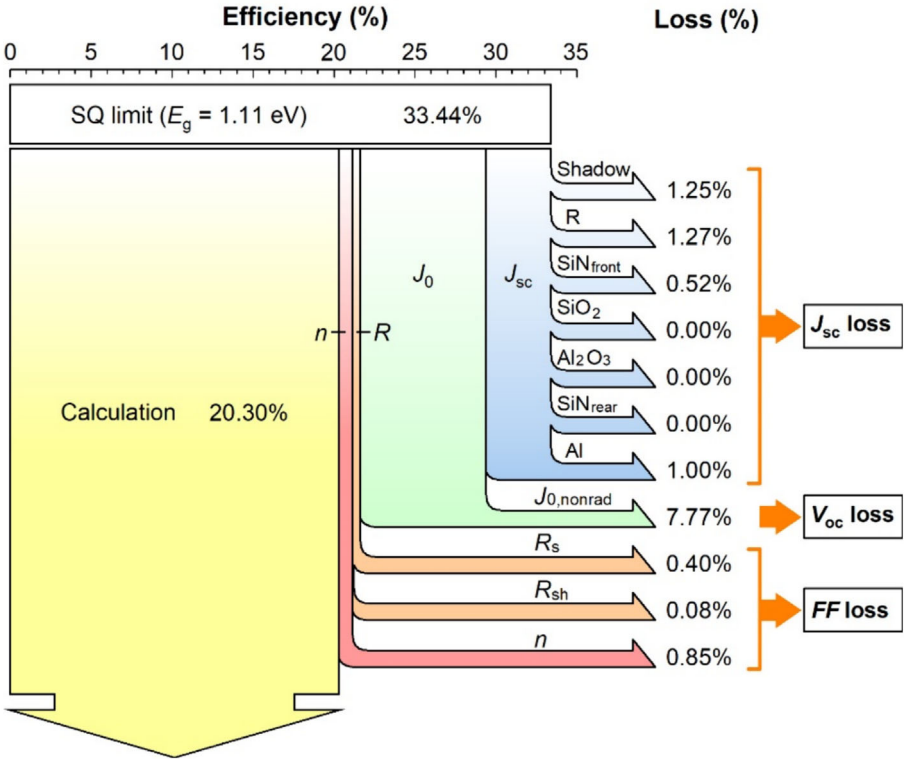

FIGURE 6 Power loss mechanism of a 20.37% efficient PERC device in Figure 1A at room temperature. The causes of the efficiency reductions are categorized by J_{sc}, V_{oc}, and FF losses. The Shockley–Queisser (SQ) limit obtained for the Si bandgap of 1.11 eV (33.44%) is also indicated. The J_{sc} loss is determined from the EQE analysis of Figure 5A, while the R in the J_{sc} loss denotes reflection loss. The efficiency loss indicated as $J_{0,nonrad}$ is caused by the increase in the nonradiative recombination. The procedure for obtaining the result can be found in Fujiwara.[49]

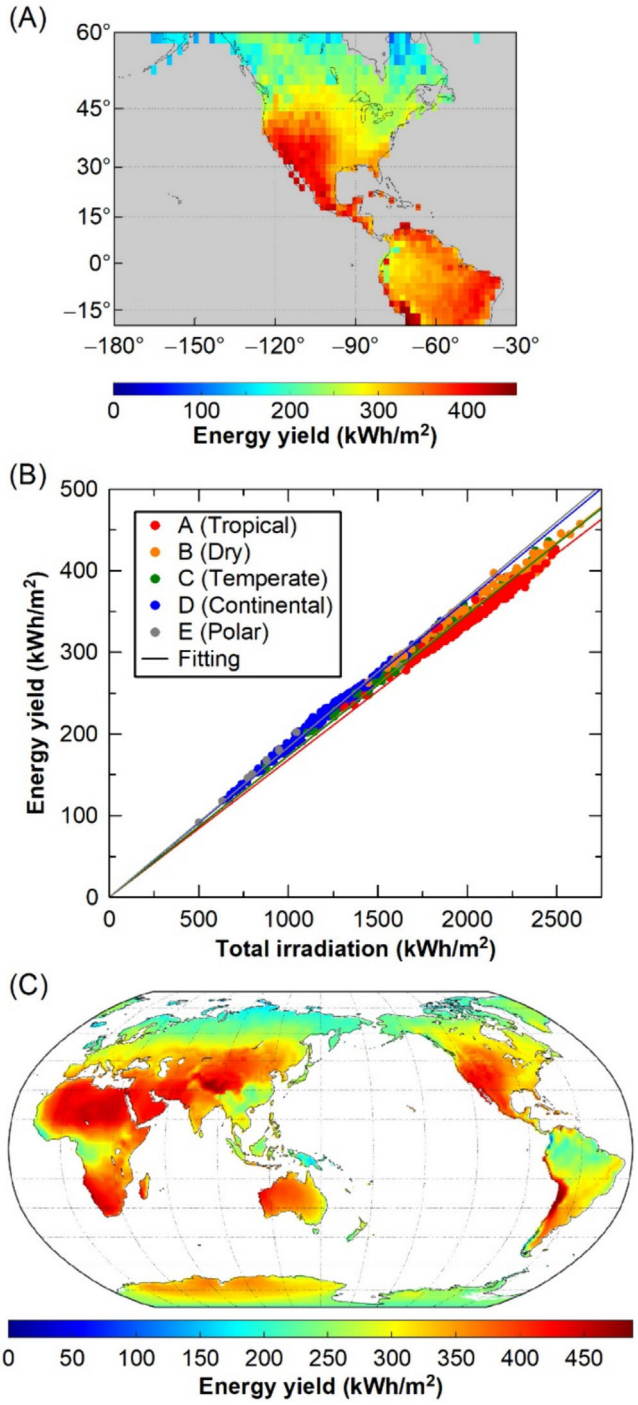

FIGURE 7 (A) Annual energy yields of the PERC module for the selected 762 places in North and South America, calculated explicitly from hourly meteorological data of each place; (B) PERC energy yield as a function of annual total sun irradiation; and (C) global energy yields of the PERC module. In (B), the energy yields in North and South America are categorized by Köppen–Geiger climate classification (A: tropical, B: dry, C: temperate, D: continental, and E: polar) and linear fittings have been performed for each climate to obtain the linear coefficients from which the global energy yield in (C) was calculated.

~400 kWh/m^2 in west-south America and Mexico region. Figure 7B summarizes the PERC energy yield as a function of annual total sun irradiation, obtained from the results of Figure 7A. In Figure 7B, the energy yields of the selected 762 places in North and South America are categorized by Köppen–Geiger climate classification (A: tropical, B: dry, C: temperate, D: continental, and E: polar), which has been adopted to interpret the performance of Si[27,58,59] and perovskite/Si[27,60] devices.

The important result derived from Figure 7B is that the PERC energy yield is essentially expressed by linear relations if the climate effect is considered properly. Specifically, as shown in Figure S7, for the regions with the same Köppen–Geiger climate classification, the annual energy yield is described quite well by $Y = C_{A\text{-}E} \times I_{total}$, where $C_{A\text{-}E}$ and I_{total} are the climate-classified yield coefficient and annual total irradiation, respectively. The actual values of $C_{A\text{-}E}$ are shown in Figure S7, and the coefficient for the tropical region ($C_A = 16.84\%$) is notably smaller than those of the cold climate regions ($C_D = 18.23\%$ and $C_E = 18.40\%$). In other words, our analysis shows that there is a maximum 10% climate effect for the annual energy yield of the PERC module, whereas the climate effect becomes smaller (~5%) in the case of the SHJ module.[27]

The results of Figure 7B indicate clearly that if the climate effect (i.e., $C_{A\text{-}E}$) and I_{total} of a calculating point are known, the annual energy yield can be calculated from the simple linear relation. From this simple method, we have predicted the global energy yield of the PERC module (Figure 7C) based on the reported I_{total} for the year 2018 (Figure S8) and Köppen–Geiger climate classification map (Figure S9). The results of Figure 7C reproduce the result obtained from the detailed calculations of Figure 7A. In a previous study,[58] a trend similar to Figure 7C has also been reported from a simpler calculation.

3.4 | Comparison with the SHJ device

Based on the results of Figure 7 obtained for the PERC module and also similar results obtained for the SHJ module, we have calculated the ratio of the PERC and SHJ energy yields ($R_y = Y_{SHJ}/Y_{PERC}$). Figure 8A shows R_y values obtained from the explicit calculations for 762 places in North and South America, categorized by Köppen–Geiger climate classification, as a function of annual total irradiation. The R_y shows a good linear relationship with the total irradiation, and R_y becomes higher in a location with a higher annual irradiation. Importantly, the climate category shows a noticeable effect on R_y. This can mainly be explained by the relationship between the average module temperature and R_y (Figure 8B). As we have seen in Figure 5D, P_{mod} ratio ($P_{mod,SHJ}/P_{mod,PERC}$) increases with T, and it can be confirmed that the P_{mod} ratio is essentially equivalent to R_y shown in Figure 8B. In the tropical region, therefore, Y_{SHJ} increases relative to Y_{PERC} due to higher operating temperatures, whereas the difference between Y_{SHJ} and Y_{PERC} shrinks in colder regions.

By applying the climate-classified yield coefficients obtained for the PERC and SHJ modules, we have calculated the global R_y shown in Figure 8C. Since uniform $C_{A\text{-}E}$ values are applied for the same

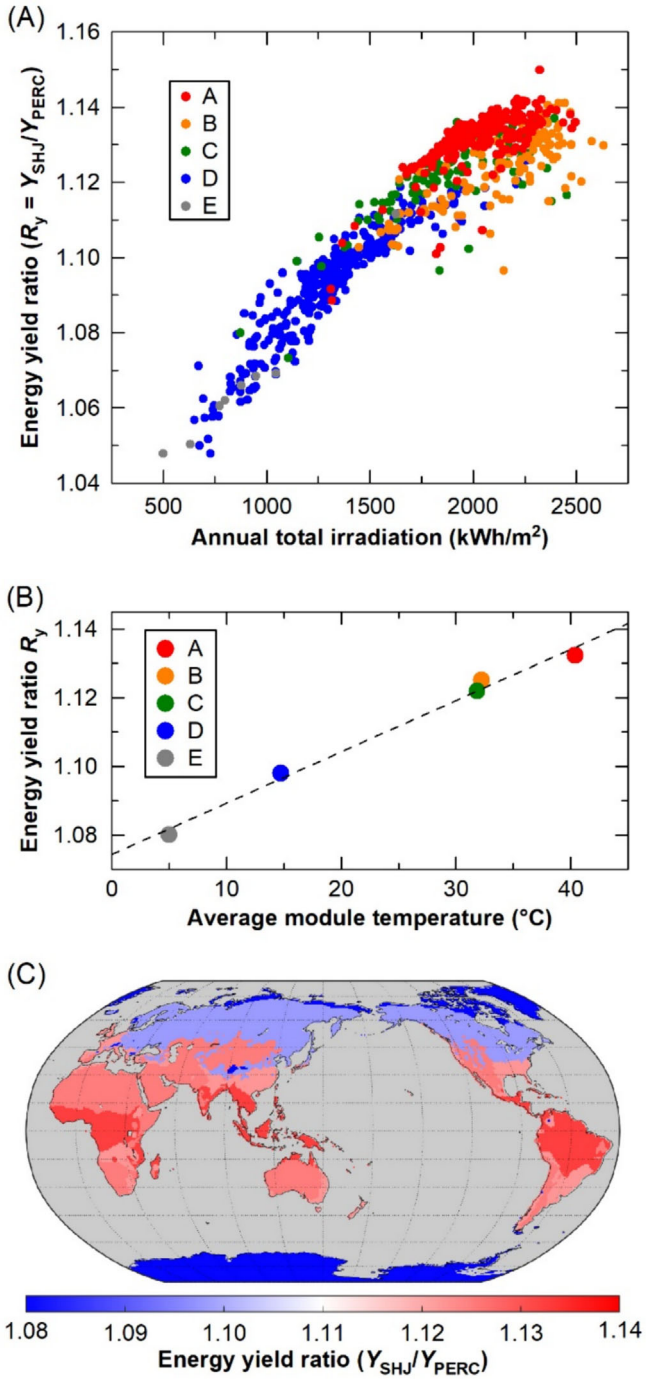

FIGURE 8 (A) Ratio of the PERC and SHJ energy yields ($R_y = Y_{SHJ}/Y_{PERC}$) calculated from the explicit calculations for 762 places in North and South America, categorized by Köppen–Geiger climate classification, as a function of the annual total irradiation; (B) relationship between average module temperature and R_y; and (C) global R_y calculated from the climate-classified yield coefficients for the PERC and SHJ modules

climate region, the obtained values are not continuous. This result shows clearly that R_y increases notably in warmer regions near equator, whereas it decreases in the Northern Hemisphere.

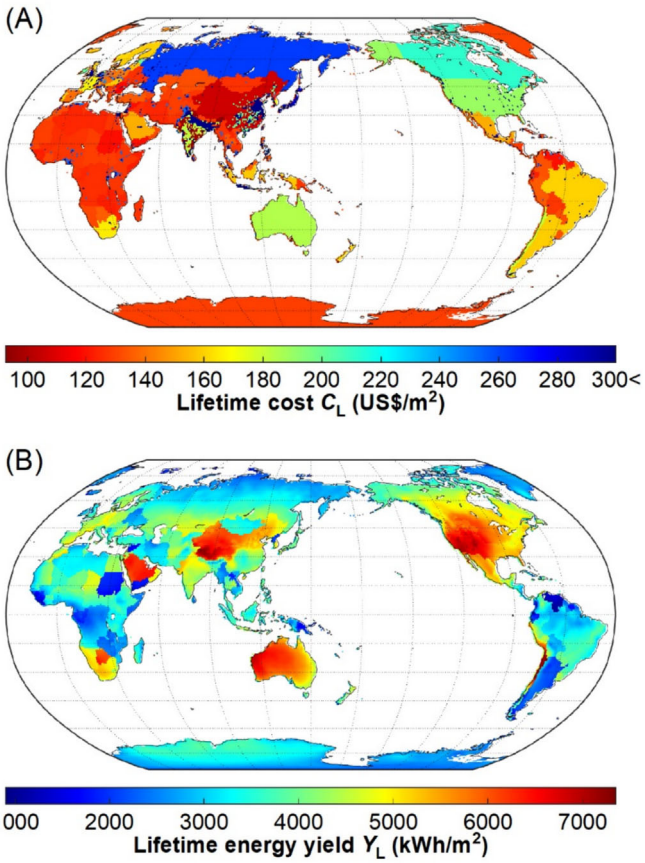

FIGURE 9 (A) Global lifetime cost (C_L) of the PERC module in 2020 US dollar and (B) global lifetime energy yield (Y_L) of the PERC module. The calculations were implemented from Equation (1) by applying country-dependent initial costs ($s_j I_{0,k}$), operation and maintenance costs ($m_j O_k$), discount rates ($r_{WACC,i}$), $U = 25$ years, Y_0 indicated in Figure 7C, and d shown in Figure 4A.

3.5 | Global LCOE

Figure 9A shows the global C_L of the PERC module for the US dollar in the year 2020, calculated from Equation (1) by applying country-dependent initial costs ($s_j I_{0,k}$), operation and maintenance costs ($m_j O_k$), country-dependent discount rates ($r_{WACC,i}$), and $U = 25$ years. In Figure 9A, an appropriate k of 1∼3 for $I_{0,k}$ and O_k was selected according to the world population density, as explained in Section 2.3. It should be emphasized that C_L differs significantly depending on the location and country. For example, C_L in Japan and Russia is quite expensive due to quite large initial investment costs ($s_j I_{0,k}$) originating from unusually high mechanical and electrical installation costs in these countries.[33] In addition, the northern area of India and east area of China exhibit very high C_L because of high population densities, which only allow the installation of expensive facilities (commercial and residential systems). In contrast, the west and central parts of China show very low C_L, as an installation cost is low in China ($s_j = 0.591$), and the utility scale facility can be placed in these areas. The United States, Australia, and many EU countries exhibit moderate C_L.

Figure 9B, on the other hand, represents the global Y_L of the PERC module, also calculated from Equation (1) using Y_0 indicated in Figure 7C, d shown in Figure 4A, and country-dependent r_j. Importantly, the global Y_L exhibits large difference from the global energy yield due to the effect of $r_{WACC,j}$. In other words, the economic situation of each country severely affects "lifetime energy yield" of solar modules, as the electricity generated by solar energy is ultimately related to the electricity retail price in each country. Specifically, in Figure 9B, we observe high Y_L only in a few countries, including the United States, China, Australia, Saudi Arabia, Chile, and Botswana, where the annual energy yields are sufficiently high with low-risk premiums (i.e., r_{risk}). Even though many African nations and central Asian nations have quite high energy yields, Y_L is not necessarily high because these countries are economically unstable. Note that Y_L in Figure 9B varies by 700% in a wide range of 1,000∼7,000 kWh/m^2, whereas C_L in Figure 9A changes in a smaller scale with a maximum 300% difference. Accordingly, it is of significant importance to consider country specific discount rate in the Y_L calculation.

Figure 10A shows the global LCOE of the PERC module for the US cent in the year 2020, obtained by dividing C_L in Figure 9A by Y_L in Figure 9B. In this figure, the global PERC LCOE is shown by selecting the utility/commercial/residential-scale installation according to the population density at each location. In Figure S10, the global PERC LCOE of utility, commercial, and residential systems are shown separately. As confirmed from Figure 10A, the LCOE depends strongly on the location and country. In particular, the LCOE map is quite different from the global energy yield shown in Figure 7C, because of the influence of socio-economic effects. In many parts of China, for example, the LCOE is quite low (<2 cents/kWh: see Figure S11), as the population density is low, the installation cost is cheaper than the United States (59.1% of the United States), and the social risk is low (i.e., $r_{WACC} = 3.78\%$) with many places exhibiting high energy yields (>400 kWh/m^2) due to abundant solar irradiation. The situation is quite similar in Saudi Arabia (Figure S11). If compared with these countries, the United States and Australia exhibit slightly higher LCOE values of ∼3 cents/kWh (Figure S11) due to higher installation costs in these countries. In addition, many European countries indicate low LCOE values of 3∼5 cents/kWh (Figure S12). In contrast, the LCOE of Japan and Russia is three to five times higher than that of the lowest region (i.e., China) because of quite high costs for solar-system installation with moderate energy yields in these regions. Sometimes, north Africa is viewed as one of the best locations to place solar panels because of quite high energy yields (400 kWh/m^2), but actual LCOE is slightly high in many African countries (3∼5 cents/kWh: Figure S12) because of high r_{WACC}. It should be emphasized that, with increasing r_{WACC}, the LCOE increases super-linearly (Figure S13). Thus, when we discuss the LCOE values in high WACC regions, the application of the country specific r_{WACC} is important.

Figure 10B represents the global LCOE of the SHJ module for the US cent in the year 2020, obtained by applying the country dependent WACC, similar to Figure 10A. In Figure S10, the global SHJ LCOE of utility, commercial, and residential systems are shown separately. Rather surprisingly, the LCOE of the SHJ module is almost the same with that of the PERC module, and there are no noticeable differences between the LCOE values in Figure 10A,B. This originates from the simple fact that the lower energy yield in the PERC module,

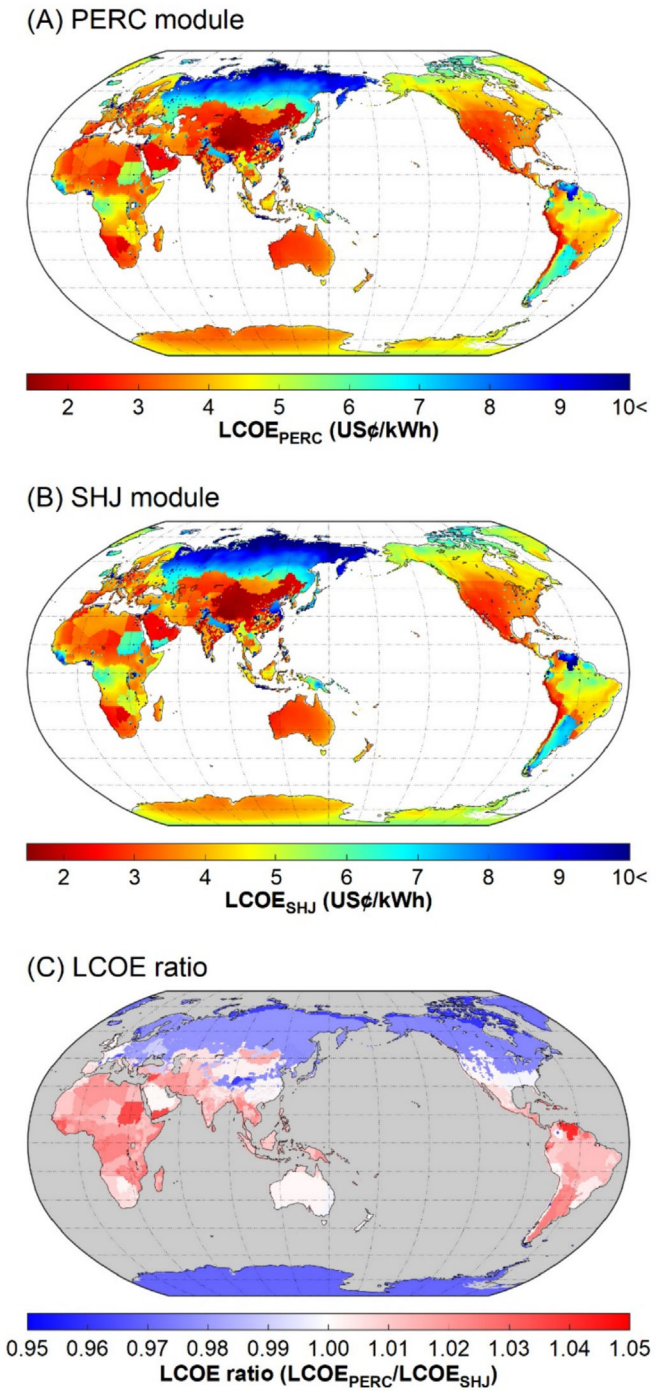

FIGURE 10 (A) Global LCOE of the PERC module for the US cent in the year 2020, calculated using $r_{WACC,j}$ expressed by Equation (2); (B) global LCOE of the SHJ module for the US cent in the year 2020, calculated using $r_{WACC,j}$ expressed by Equation (2); and (C) LCOE ratio (R_{LCOE} = LCOE$_{PERC}$/LCOE$_{SHJ}$) calculated from the results of (A) and (B). In (A), the result was obtained by dividing C_L in Figure 9A by Y_L in Figure 9B. The global LCOE is determined by selecting the utility/commercial/residential-scale capacity according to the population density at each location.

relative to the SHJ module, is compensated by the lower system cost of the PERC system, resulting in the similar installation costs for both the PERC and SHJ modules.

In a global scale, however, there are slight differences in the cost performance between the PERC and SHJ modules. In Figure 10C, the LCOE ratio of $R_{LCOE} = LCOE_{PERC}/LCOE_{SHJ}$ is shown with the colors of white for $R_{LCOE} = 1$, red for $R_{LCOE} > 1$, and blue for $R_{LCOE} < 1$. In the United States, China, Saudi Arabia, and Australia, $R_{LCOE} \sim 1$, and, therefore, the PERC and SHJ modules exhibit similar cost efficiencies. Nevertheless, in the regions near equator, R_{LCOE} increases because the LCOE of the SHJ module becomes relatively smaller, compared with the PERC module, whereas in the Northern Hemisphere, the trend is opposite. This result is consistent with that shown in Figure 8A; in the equator region, the energy yield of the SHJ device becomes higher than that of the PERC structure, as the low temperature coefficient of the SHJ cells is beneficial at high operating temperatures in these regions, while in the colder regions, the lower cost of the PERC modules becomes more advantageous in lowering the LCOE. Accordingly, there is a slight preference for the choice of the PERC/SHJ modules across the globe.

4 | DISCUSSION

4.1 | LCOE of the PERC and SHJ modules

By applying the recent cost estimate and the state-of-the-art module structures, we have confirmed that the LCOE of the PERC and SHJ modules is in a range of 3∼6 cents/kWh in many countries. It should be emphasized that these LCOE values are significantly lower than those reported in earlier studies,[13,15,16] as the LCOE of solar energy decreased remarkably in the last decade[33] due to the intense R&D and investment on solar modules.[6] In fact, in a recent attempt to obtain global LCOE for a solar module based on a simplified method, a similar LCOE of 2∼5 cents/kWh has been estimated.[14]

Rather surprisingly, the actual LCOE of a solar system (600 MW) installed in Saudi Arabia in 2021 is as low as 1 cent/kWh.[33] This lower LCOE, compared with our estimation (∼2.5 cents/kWh), can be interpreted by the larger installation size (600 MW) than our assumption (100 MW), which help to reduce the installation cost.

Importantly, the above LCOE of solar systems is notably lower, compared with those of a natural-gas power plant (>4.5 cents/kWh in gas combined cycle), coal power plant (>6.5 cents/kWh), and nuclear plant (>13 cents/kWh).[5] In the case of a carbon-capture and storage (CCS) facility for a coal plant, a very high cost (>15 cents/kWh) has been estimated.[5,61] Accordingly, renewable energies including solar PV and wind energy (LCOE ∼3 cents/kWh)[5] have a clear and obvious cost merit. Nevertheless, one disadvantage of solar and wind systems is a high capital cost for initial installation,[9,62] and thus, financial support particularly to developing countries is important as discussed widely.[9,62,63]

In our LCOE estimation, on the other hand, slight power-generation losses caused by dirt (dust) formation on module panels and a power conditioner have been neglected; thus, our LCOE is slightly underestimated by considering only ideal conditions. However, for the utility and commercial-scale systems, cleaning of solar modules has been incorporated as the maintenance cost.

In this study, only monofacial configuration, rather than bifacial configuration, has been considered to avoid the complexity of bifacial optical simulations. In commercial SHJ modules, the bifacial configuration becomes a standard and the energy yield of a bifacial SHJ system becomes higher by 8%, compared with a monofacial system,[20] due to the photocarrier generation from the backside illumination. A similar increase in the energy yield is observed for a bifacial PERC device.[64] Thus, the LCOE of the bifacial modules is expected to become lower by ∼8%, compared with the monofacial structures.

The suppression of the cell degradation shown in Figure 4 is also important to further reduce the LCOE. In recent PERC solar modules,[7,40] Ga-doped Si wafers, instead of B-doped Si wafers, are adopted to suppress the light-induced degradation observed in B-doped Si wafers.[65,66] However, some results show that Ga-doped devices are still not completely immune to light-induced degradation, most likely due to the presence of residual impurities including B.[40,67] Accordingly, more quantitative data are necessary to discuss the influence of the suppressed degradation in Ga-doped PERC devices on their LCOE.

It should be noted that the strong degradation in SHJ devices shown in Figure 4 has been observed consistently[44,68] and should be considered universal. The degradation of SHJ solar panels is caused primarily by the degradation of V_{oc}.[68] As well known, a-Si:H layers incorporated as passivation layers in SHJ devices exhibit quite strong photo-induced degradation,[69] and the defect concentration in a-Si:H increases significantly by light illumination.[70] Such light-induced defect generation has been found to be connected to the generation of local SiH_2 bonding formed in amorphous network.[71,72] Importantly, Fujiwara and Kondo[73] found the presence of significant SiH_2-rich structure at a-Si:H/c-Si interface. Thus, we suggest that the light illumination leads to the notable defect generation at the SiH_2-rich interface, which in turn increases the carrier recombination at the hetero-interface, decreasing V_{oc} of SHJ cells. As confirmed from the result of Figure 4, the suppression of the SHJ degradation is quite impactful for the improvement of the LCOE.

4.2 | LCOE of solar energy in near future

International energy agency (IEA) predicts that the LCOE of solar PV continues to decrease and becomes less than half in 2050.[74] In fact, recent developments in Si cell fabrication technology improve the cell efficiency steadily[75–78] and likely contribute to lower cell manufacturing costs. Specifically, to improve the V_{oc} loss caused by large J_0 in PERC devices (Figure 6), a tunnel-oxide-passivated-contacts (TOPCon) solar cell,[75] exhibiting a quite high efficiency of 26.7%,[78] has been developed, and the bifacial TOPCon structure is expected to improve the cost performance of solar PV.

Moreover, solar PV has been exhibiting a remarkable cost reduction in a long term with a quite large learning rate (price experience curve) of 40% during 2006–2020.[7] As discussed previously,[2,79] such high learning rates have been observed widely in semiconductor industries (40% for DRAM chips and 35% for flat panel display). Accordingly, it appears that solar PV has an intrinsically high learning rate and the realization of the cost reduction by scaling up the production volume is an important feature of PV industry, given that sufficient R&D efforts continue.

4.3 | Super grid

The global LCOE obtained in this study (Figure 10) indicates clearly that the LCOE varies quite significantly depending on the location and country. More importantly, several countries (China, Saudi Arabia, the United States, Australia, and Chile) exhibit very low LCOE (2∼3 cents/kWh), while other countries show moderate LCOEs (3∼6 cents/kWh). One possible way to lower the LCOE in moderate- and high-LCOE countries is an installation of intergovernmental grids (i.e., so-called "super grid").[80,81] For example, the LCOE of Japan and Korea is rather expensive, and, if an intercontinental grid is formed between China-Korea-Japan, the overall LCOE is expected to decrease notably, although the installation of high-voltage DC lines across the continent increases the LCOE slightly.[80] This "super grid" is quite promising to increase the resilience of time- and season-varying renewable energy sources, while reducing the net capacity for storage (i.e., batteries). Indeed, the formation of the intergovernmental grid is a vital solution for small nations with high population densities (Japan and Singapore, for example) to build a renewable-energy-dominant society.

At this stage, the utilization of solar energy for H_2 production by water splitting has gained significant attraction in numerous countries as a pivotal approach toward decarbonizing society.[82–84] In this case, however, the cost of H_2 production is determined essentially by the LCOE of renewable energy, and the difference of the LCOE influences the competitiveness of a H_2 energy source. The low-LCOE countries can be net H_2 exporters, but the long-distance transmission of H_2 has a technological challenge due to a low energy density of H_2.[85] Moreover, the overall efficiency of H_2 production by water splitting and the following electricity generation by fuel cells is not so high.[86] Thus, in the view of these technological aspects, the super-grid concept is quite preferable, even though there exists political challenge in realizing super-grid approach.

5 | CONCLUSION

To determine global LCOE for the two types of solar modules with the PERC and SHJ configurations, we have developed a new scheme that includes important features of (i) accurate calculation of solar-module energy yields based on full spectral and meteorological-data consideration and (ii) global-LCOE estimation according to a population density for determining an installation capacity (utility/commercial/residential system) as well as country-specific capital costs and discount rates. For the LCOE calculation of a PERC module, we have fully modeled the temperature-dependent EQE and *J-V* characteristics of a 20%-efficient PERC device, from which critical device-operating parameters are extracted. Our optical and *J-V* simulation methods provide almost perfect fitting to the temperature varying EQE and *J-V* characteristics. The detailed energy yield calculations performed for the PERC module at 762 places in North and South America show that the energy yield has an essentially linear relationship with the annual total irradiation. However, we observe the notable temperature effect on the PERC energy yield, and our analysis based on Köppen–Geiger classification shows clearly that the climate (temperature) effect on the PERC module performance is 10%; specifically, colder regions exhibit superior performance, if compared with warmer regions. Based on similar analyses performed for a 23%-efficient SHJ device in our previous study, we find that the SHJ energy yield becomes higher in regions near equator, compared with the PERC energy yield, due to a lower temperature coefficient of the SHJ device, whereas the advantages of the SHJ device diminish in the colder regions in the Northern Hemisphere.

We have carried out quite detailed LCOE calculations for the PERC and SHJ modules for three different installation capacities of 100 MW (utility), 500 kW (commercial), and 5 kW (residential) and have obtained the global LCOE by selecting the proper system size for each place according to the population density. As a result, we find a very low LCOE of <3 cents/kWh for 2020 US dollar in many parts of China, Saudi Arabia, the United States, Australia, Chile, and Botswana because of high energy yields, low population densities, low capital costs, and low-country risk premiums (WACC) in these countries, whereas many European countries exhibit a moderate LCOE of 3∼5 cents/kWh. In contrast, the LCOE values in Japan and Russia are quite high primary due to very high initial installation costs with moderate energy yields. Interestingly, the LCOE values of the PERC and SHJ modules are found to be very similar. In the regions near equator, however, the SHJ module exhibits a better cost performance due to superior temperature coefficient, whereas in the Northern Hemisphere, the cost performance of the PERC module becomes better, as the module fabrication cost is lower, compared with the SHJ module.

ACKNOWLEDGEMENTS

The authors acknowledge Drs. Yoshihiro Hishikawa and Masahiro Yoshita of National Institute of Advanced Industrial Science and Technology (AIST) for their contribution of measuring temperature dependent *J-V* and EQE of the Si PERC device. The authors also thank Mao Iida and Takumi Oka for the assistance concerning data interpretation.

CONFLICT OF INTEREST STATEMENT

The authors declare no conflict of interest.

DATA AVAILABILITY STATEMENT

The data of this study are available from the corresponding author upon reasonable request.

REFERENCES

1. Branker K, Pathak MJM, Pearce JM. A review of solar photovoltaic levelized cost of electricity. *Renew. Sustain. Energy Rev.* 2011;15(9):4470-4482. doi:10.1016/j.rser.2011.07.104
2. Breyer C, Gerlach A. Global overview on grid-parity. *Progr. Photovolt.: Res. Appl.* 2013;21(1):121-136. doi:10.1002/pip.1254
3. Fraunhofer ISE. 2015 Current and future cost of photovoltaics. Long-term scenarios for market development, system prices and LCOE of utility-scale PV systems. Study on behalf of Agora Energiewende. https://www.agora-energiewende.de/en/publications/current-and-future-cost-of-photovoltaics/
4. Kost C, Shammugam S, Fluri V, et al. *Levelized Cost of Electricity-Renewable Energy Technologies (June 2021)*. Fraunhofer ISE; 2021. https://www.ise.fraunhofer.de/en/publications/studies/cost-of-electricity.html
5. Lazard. *Lazard's Levelized Cost of Energy Analysis—Version 15.0*. Lazard; 2021. https://www.lazard.com/media/sptlfats/lazards-levelized-cost-of-energy-version-150-vf.pdf
6. Kavlak G, McNerney J, Trancik JE. Evaluating the causes of cost reduction in photovoltaic modules. *Energy Policy*. 2018;123:700-710. doi:10.1016/j.enpol.2018.08.015
7. ITRPV. International Technology Roadmap for Photovoltaic (ITRPV): 2020 results 2021. http://www.itrpv.net/Reports/Downloads/
8. IEA. *Renewable Energy Market Update—June 2023*. IEA; 2023. https://www.iea.org/reports/renewable-energy-market-update-june-2023
9. Creutzig F, Agoston P, Goldschmidt JC, Luderer G, Nemet G, Pietzcker RC. The underestimated potential of solar energy to mitigate climate change. *Nat. Energy*. 2017;2(9):17140. doi:10.1038/nenergy.2017.140
10. Messmer C, Goraya BS, Nold S, et al. The race for the best silicon bottom cell: efficiency and cost evaluation of perovskite–silicon tandem solar cells. *Prog. Photovolt.: Res. Appl.* 2021;29(7):744-759. doi:10.1002/pip.3372
11. Zafoschnig LA, Nold S, Goldschmidt JC. The race for lowest costs of electricity production: techno-economic analysis of silicon, perovskite and tandem solar cells. *IEEE J. Photovolt.* 2020;10(6):1632-1641. doi:10.1109/JPHOTOV.2020.3024739
12. Ramasamy V, Feldman D, Desai J, Margolis RUS. *Solar Photovoltaic System and Energy Storage Cost Benchmarks: Q1 2021*. National Renewable Energy Laboratory; 2021. doi:10.2172/1829460
13. Ondraczek J, Komendantova N, Patt A. WACC the dog: the effect of financing costs on the levelized cost of solar PV power. *Renew. Energy*. 2015;75:888-898. doi:10.1016/j.renene.2014.10.053
14. Kan X, Reichenberg L, Hedenus F, Daniels D. Global renewable LCOE—including socio-economic factors in assessments of resource potential. *arXiv Preprint*. 2022. 10.48550/arXiv.2202.02257
15. Suri M, Betak J, Rosina K, et al. *Global Photovoltaic Power Potential by Country*. World Bank; 2020. doi:10.1596/34102
16. Joshi S, Mittal S, Holloway P, Shukla PR, Ó Gallachóir B, Glynn J. High resolution global spatiotemporal assessment of rooftop solar photovoltaics potential for renewable electricity generation. *Nat. Commun.* 2021;12(1):5738. doi:10.1038/s41467-021-25720-2
17. Green MA. The passivated emitter and rear cell (PERC): from conception to mass production. *Sol. Energy Mater. Sol. Cells*. 2015;143:190-197. doi:10.1016/j.solmat.2015.06.055
18. Dullweber T, Schmidt J. Industrial silicon solar cells applying the passivated emitter and rear cell (PERC) concept—a review. *IEEE J. Photovolt.* 2016;6(5):1366-1381. doi:10.1109/JPHOTOV.2016.2571627
19. Altermatt PP, Xiong Z, He Q, et al. High-performance p-type multicrystalline silicon (mc-Si): its characterization and projected performance in PERC solar cells. *Sol. Energy*. 2018;175:68-74. doi:10.1016/j.solener.2018.01.073
20. Taguchi M, Kawamoto K, Tsuge S, et al. HIT™ cells—high-efficiency crystalline Si cells with novel structure. *Progr. Photovolt.: Res. Appl.* 2000;8(5):503-513. doi:10.1002/1099-159X(200009/10)8:53.0.CO;2-G
21. Taguchi M, Terakawa A, Maruyama E, Tanaka M. Obtaining a higher V_{oc} in HIT cells. *Progr. Photovolt.: Res. Appl.* 2005;13(6):481-488. doi:10.1002/pip.646
22. Lin H, Yang M, Ru X, et al. Silicon heterojunction solar cells with up to 26.81% efficiency achieved by electrically optimized nanocrystalline-silicon hole contact layers. *Nat. Energy*. 2023;8(8):789-799. doi:10.1038/s41560-023-01255-2
23. Trina Solar. 210 PERC cell efficiency achieves 24.5%, Trina Solar breaks world record for the 24th time. 2022. Accessed July 2023. https://www.trinasolar.com/en-glb/resources/newsroom/en210-perc-cell-efficiency-achieves-245-trina-solar-breaks-world-record-24th-time
24. Jinko Solar. Product data sheet of "Cheetah HC 72M 390–410".
25. Canadian Solar. Product data sheet of "KuMax CS3U-375/380MS".
26. Adani Solar. Product data sheet of "ASM-7-PERC-375".
27. Kato Y, Katayama H, Kobayashi T, et al. Global prediction of the energy yields for hybrid perovskite/Si tandem and Si heterojunction single solar modules. *Prog. Photovolt.: Res. Appl.* 2022;30(10):1198-1218. doi:10.1002/pip.3569
28. Fujiwara H, Collins RW. Spectroscopic ellipsometry for photovoltaics. In: *Applications and Optical Data of Solar Cell Materials*. Vol.2. Springer; 2018. doi:10.1007/978-3-319-95138-6
29. National Renewable Energy Laboratory. NSRDB data viewer. Accessed January 2021. https://maps.nrel.gov/nsrdb-viewer
30. Xie Y, Sengupta M. A fast all-sky radiation model for solar applications with narrowband irradiances on tilted surfaces (FARMS-NIT): part I. The clear-sky model. *Sol. Energy*. 2018;174:691-702. doi:10.1016/j.solener.2018.09.056
31. Xie Y, Sengupta M, Wang C. A fast all-sky radiation model for solar applications with narrowband irradiances on tilted surfaces (FARMS-NIT): part II. The cloudy-sky model. *Sol. Energy*. 2019;188:799-812. doi:10.1016/j.solener.2019.06.058
32. European Central Bank. Euro foreign exchange reference rates. Accessed March 2023. https://www.ecb.europa.eu/stats/policy_and_exchange_rates/euro_reference_exchange_rates/html/eurofxref-graph-usd.en.html
33. IRENA. *Renewable Power Generation Costs in 2020*. International Renewable Energy Agency; 2021. https://www.irena.org/publications/2021/Jun/Renewable-Power-Costs-in-2020
34. Egli F, Steffen B, Schmidt TS. Bias in energy system models with uniform cost of capital assumption. *Nat. Commun.* 2019;10(1):4588. doi:10.1038/s41467-019-12468-z
35. Bogdanov D, Child M, Breyer C. Reply to 'Bias in energy system models with uniform cost of capital assumption'. *Nat. Commun.* 2019;10(1):4587. doi:10.1038/s41467-019-12469-y
36. IEA. *World Energy Outlook 2016*. IEA; 2016. https://www.iea.org/reports/world-energy-outlook-2016
37. IRENA. *Renewable Power Generation Costs in 2021*. International Renewable Energy Agency; 2022. https://www.irena.org/publications/2022/Jul/Renewable-Power-Generation-Costs-in-2021
38. Egli F, Steffen B, Schmidt TS. Learning in the financial sector is essential for reducing renewable energy costs. *Nat. Energy*. 2019;4(10):835-836. doi:10.1038/s41560-019-0482-3
39. Damodaran A. Damodaran ONLINE, data: archives. Accessed March 2023. https://pages.stern.nyu.edu/~adamodar/New_Home_Page/dataarchived.html

40. Chen C, Wang H, Wang J, Lv J, Yang H. Performance degradation of commercial Ga-doped passivated emitter and rear cell solar modules in the field. *Progr. Photovolt.: Res. Appl.* 2022;30(3):300-309. doi:10.1002/pip.3512
41. ITRPV. International Technology Roadmap for Photovoltaic (ITRPV). 2018 results. 2019. http://www.itrpv.net/Reports/Downloads/
42. LONGi Solar. Product data sheet of "LR4-60HPH-365∼385M".
43. Jordan DC, Kurtz SR. Photovoltaic degradation rates—an analytical review. *Prog. Photovolt.: Res. Appl.* 2013;21(1):12-29. doi:10.1002/pip.1182
44. Jordan DC, Kurtz SR, VanSant K, Newmiller J. Compendium of photovoltaic degradation rates. *Prog. Photovolt.: Res. Appl.* 2016;24(7):978-989. doi:10.1002/pip.2744
45. United States Census Bureau. *Urban Area Criteria for the 2010 Census. Federal Register (Vol. 76, No. 164)*. US Government Publishing Office; 2011. https://www2.census.gov/geo/pdfs/reference/fedreg/fedregv76n164.pdf
46. Center for International Earth Science Information Network (CIESIN). *Documentation for Gridded Population of the World, Version 4 (GPWv4), Revision 11 Data Sets*. NASA Socioeconomic Data and Applications Center (SEDAC); 2018. doi:10.7927/H45Q4T5F
47. Lautenschlager P, Garriga M, Vina L, Cardona M. Temperature dependence of the dielectric function and interband critical points in silicon. *Phys. Rev. B*. 1987;36(9):4821-4830. doi:10.1103/PhysRevB.36.4821
48. Nishigaki Y, Nagai T, Nishiwaki M, et al. Extraordinary strong band-edge absorption in distorted chalcogenide perovskites. *Sol. RRL*. 2020;4(5):1900555. doi:10.1002/solr.201900555
49. Fujiwara H. *Hybrid Perovskite Solar Cells: Characteristics and Operation*. Wiley-VCH; 2022. doi:10.1002/9783527825851
50. Tiedje T, Yablonovitch E, Cody GD, Brooks BG. Limiting efficiency of silicon solar cells. *IEEE Trans. Electron. Devices*. 1984;31(5):711-716. doi:10.1109/T-ED.1984.21594
51. Green MA. Limits on the open-circuit voltage and efficiency of silicon solar cells imposed by intrinsic Auger processes. *IEEE Trans. Electron. Devices*. 1984;31(5):671-678. doi:10.1109/T-ED.1984.21588
52. Richter A, Glunz SW, Werner F, Schmidt J. Improved quantitative description of auger recombination in crystalline silicon. *Phys. Rev. B*. 2012;86(16):165202. doi:10.1103/PhysRevB.86.165202
53. Haschke J, Seif JP, Riesen Y, et al. The impact of silicon solar cell architecture and cell interconnection on energy yield in hot & sunny climates. *Energ. Environ. Sci.* 2017;10(5):1196-1206. doi:10.1039/C7EE00286F
54. Taguchi M, Maruyama E, Tanaka M. Temperature dependence of amorphous/crystalline silicon heterojunction solar cells. *Jpn. J. Appl. Phys.* 2008;47(2):814-818. doi:10.1143/JJAP.47.814
55. Shockley W, Queisser HJ. Detailed balance limit of efficiency of p-n junction solar cells. *J. Appl. Phys.* 1961;32(3):510-519. doi:10.1063/1.1736034
56. Richter A, Hermle M, Glunz SW. Reassessment of the limiting efficiency for crystalline silicon solar cells. *IEEE J. Photovolt.* 2013;3(4):1184-1191. doi:10.1109/JPHOTOV.2013.2270351
57. Brendel R, Dullweber T, Peibst R, Kranz C, Merkle A, Walter D. Breakdown of the efficiency gap to 29% based on experimental input data and modeling. *Prog. Photovolt.: Res. Appl.* 2016;24(12):1475-1486. doi:10.1002/pip.2696
58. Peters IM, Buonassisi T. Energy yield limits for single-junction solar cells. *Joule*. 2018;2(6):1160-1170. doi:10.1016/j.joule.2018.03.009
59. Ascencio-Vásquez J, Brecl K, Topič M. Methodology of Köppen-Geiger-photovoltaic climate classification and implications to worldwide mapping of PV system performance. *Sol. Energy*. 2019;191:672-685. doi:10.1016/j.solener.2019.08.072
60. Liu H, Rodríguez-Gallegos CD, Liu Z, Buonassisi T, Reindl T, Peters IM. A worldwide theoretical comparison of outdoor potential for various silicon-based tandem module architecture. *Cell. Rep. Phys. Sci.* 2020;1(4):100037. doi:10.1016/j.xcrp.2020.100037
61. Agora Energiewende. Comparing the cost of low-carbon technologies: What is the cheapest option?. report by Prognos AG on behalf of Agora Energiewende. 2014. www.prognos.com/fileadmin/pdf/publikationsdatenbank/140417_Prognos_Agora_Analysis_Decarbonisationtechnologies_EN.pdf
62. Schmidt TS. Low-carbon investment risks and de-risking. *Nat. Clim. Chang.* 2014;4(4):237-239. doi:10.1038/nclimate2112
63. IEA. *Financing Clean Energy Transitions in Emerging and Developing Economies*. IEA; 2021. https://www.iea.org/reports/financing-clean-energy-transitions-in-emerging-and-developing-economies
64. Dullweber T, Schulte-Huxel H, Blankemeyer S, et al. Present status and future perspectives of bifacial PERC+ solar cells and modules. *Jan. J. Appl. Phys.* 2018;57(8S3):08RA01. doi:10.7567/JJAP.57.08RA01
65. Bothe K, Sinton R, Schmidt J. Fundamental boron-oxygen-related carrier lifetime limit in mono- and multicrystalline silicon. *Progr. Photovolt.: Res. Appl.* 2005;13(4):287-296. doi:10.1002/pip.586
66. Glunz SW, Rein S, Lee JY, Warta W. Minority carrier lifetime degradation in boron-doped Czochralski silicon. *J. Appl. Phys.* 2001;90(5):2397-2404. doi:10.1063/1.1389076
67. Grant NE, Altermatt PP, Niewelt AT, et al. Gallium-doped silicon for high-efficiency commercial passivated emitter and rear solar cells. *Sol. RRL*. 2021;5(4):2000754. doi:10.1002/solr.202000754
68. Ishii T, Masuda A. Annual degradation rates of recent crystalline silicon photovoltaic modules. *Prog. Photovolt.: Res. Appl.* 2017;25(12):953-967. doi:10.1002/pip.2903
69. Staebler DL, Wronski CR. Reversible conductivity changes in discharge-produced amorphous Si. *Appl. Phys. Lett.* 1977;31(4):292-294. doi:10.1063/1.89674
70. Street RA. *Hydrogenated amorphous silicon*. Cambridge Univ. Press; 1991. doi:10.1017/CBO9780511525247
71. Bhattacharya E, Mahan AH. Microstructure and the light-induced metastability in hydronated amorphous silicon. *Appl. Phys. Lett.* 1988;52(19):1587-1589. doi:10.1063/1.99098
72. Nakamura N, Takahama T, Isomura M, et al. The influence of the Si-H_2 bond on the light-induced effect in a-Si films and a-Si solar cells. *Jpn. J. Appl. Phys.* 1989;28(10R):1762. doi:10.1143/JJAP.28.1762
73. Fujiwara H, Kondo M. Effects of a-Si:H layer thicknesses on the performance of a-Si:H/c-Si heterojunction solar cells. *J. Appl. Phys.* 2007;101:054516. doi:10.1063/1.2559975
74. IEA. *Net Zero by 2050: A Roadmap for the Global Energy Sector*. IEA; 2021. https://www.iea.org/reports/net-zero-by-2050
75. Feldmann F, Bivour M, Reichel C, Hermle M, Glunz SW. Passivated rear contacts for high-efficiency n-type Si solar cells providing high interface passivation quality and excellent transport characteristics. *Sol. Energy Mater. Sol. Cells*. 2014;120:270-274. doi:10.1016/j.solmat.2013.09.017
76. Chen Y, Chen D, Liu C, et al. Mass production of industrial tunnel oxide passivated contacts (i-TOPCon) silicon solar cells with average efficiency over 23% and modules over 345 W. *Prog. Photovoltaics*. 2019;27(10):827-834. doi:10.1002/pip.3180
77. Chen D, Chen Y, Wang Z, et al. 24.58% total area efficiency of screen-printed, large area industrial silicon solar cells with the tunnel oxide passivated contacts (i-TOPCon) design. *Sol. Energy Mater. Sol. Cells*. 2020;206:110258. doi:10.1016/j.solmat.2019.110258
78. Bellini E. 2023. Jolywood claims 26.7% efficiency for n-type TOPCon solar cell. Accessed July 2023. PV Magazine: 12 April 2023. https://www.pv-magazine.com/2023/04/12/jolywood-claims-26-7-efficiency-for-n-type-topcon-solar-cell/
79. Hoffmann W, Wieder S, Pellkofer T. Differentiated price experience curves as evaluation tool for judging the further development of crystalline silicon and thin film PV solar electricity products. 24th European Photovoltaic Solar Energy Conference: Hamburg; 2009.
80. Bogdanov D, Breyer C. North-East Asian super grid for 100% renewable energy supply: optimal mix of energy technologies for electricity,

gas and heat supply options. *Energ. Conver. Manage.* 2016;112:176-190. doi:10.1016/j.enconman.2016.01.019

81. Wang M, An T, Ergun H, et al. Review and outlook of HVDC grids as backbone of transmission system. *CSEE J. Power Energy Syst.* 2020;7(4):797-810. doi:10.17775/CSEEJPES.2020.04890
82. Staffell I, Scamman D, Abad AV, et al. The role of hydrogen and fuel cells in the global energy system. *Energ. Environ. Sci.* 2019;12(2):463-491. doi:10.1039/C8EE01157E
83. WEC. *Innovation Insights Briefing: Hydrogen on the Horizon: Ready, Almost Set, Go?* World Energy Council; 2021. https://www.worldenergy.org/publications/entry/innovation-insights-brief-hydrogen-on-the-horizon-ready-almost-set-go
84. IEA. *Global Hydrogen Review 2022*. IEA; 2022. https://www.iea.org/reports/global-hydrogen-review-2022
85. IEA. *The Future of Hydrogen*. IEA; 2019. https://www.iea.org/reports/the-future-of-hydrogen
86. Jacobson MZ. *100% Clean, Renewable Energy and Storage for Everything*. Cambridge University Press; 2020. doi:10.1017/9781108786713

SUPPORTING INFORMATION

Additional supporting information can be found online in the Supporting Information section at the end of this article.

How to cite this article: Kobayashi T, Katayama H, Kinden Y, et al. Cost-efficiency potential of solar energy on a global scale: Case studies for Si solar modules with PERC and heterojunction structures. *Prog Photovolt Res Appl*. 2024;32(11):799-813. doi:10.1002/pip.3835